Journal of Materials Chemistry A

PAPER

View Article Online
View Journal | View Issue

Cite this: J. Mater. Chem. A, 2015, 3, 24281

Atomically precise growth of sodium titanates as anode materials for high-rate and ultralong cycle-life sodium-ion batteries†

Jian Liu,[ab] Mohammad N. Banis,[a] Biwei Xiao,[a] Qian Sun,[a] Andrew Lushington,[a] Ruying Li,[a] Jinghua Guo,[bd] Tsun-Kong Sham[c] and Xueliang Sun*[a]

Received 20th October 2015
Accepted 5th November 2015

DOI: 10.1039/c5ta08435k

www.rsc.org/MaterialsA

Sodium-ion batteries (SIBs) have received increasing attention for applications in large-scale energy storage systems due to their low cost, high energy density, and high abundance of the sodium element. Nanosizing electrode materials becomes a key strategy to overcome the problems resulting from the sluggish kinetics of large sodium ions, thereby achieving good performance in SIBs. Herein, we developed an atomic layer deposition (ALD) approach for atomically precise fabrication of sodium titanate anode materials. This ALD process shows excellent controllability over the growth rate, film thickness, composition of sodium titanates, and high flexibility of coating uniform sodium titanate films onto various dimensions of substrates. Moreover, the amorphous sodium titanate deposited on carbon nanotubes exhibits high specific capacity, excellent rate capability, and ultra-long cycling life (~100 mA h g^{-1} after 3500 cycles). It is expected that the ALD approach developed herein can be extended to well-defined fabrication of other sodium-containing electrode materials for SIBs.

Introduction

Lithium-ion batteries (LIBs) have become the predominant battery technology for portable electronic devices, and are considered as the most promising energy storage systems for the next generation of electric vehicles (EVs).[1–3] However, the growing market for LIBs has raised concerns about the feasibility of lithium, due to its low abundance in the Earth's crust (0.006 wt%).[4,5] The increasing demand for lithium-containing electrode materials will drive up the price of lithium precursors (such as Li_2CO_3), ultimately making lithium-ion technology expensive. In this regard, sodium-ion batteries (SIBs) have attracted increasing attention from researchers, because of the high abundance of sodium (2.4 wt% on Earth), and the wide availability and low cost of sodium precursors.[4] Moreover, sodium is the second lightest and smallest alkali metal, with an electrochemical potential of −2.71 V *versus* standard hydrogen electrode (just 0.3 V higher than that of Li^+/Li).[4–6] Although the slightly higher electrochemical potential results in somewhat lower energy and power density of SIBs than LIBs, it is still a good choice for energy storage applications where low cost is more preferable. All these characteristics make SIBs an ideal alternative to LIBs for large-scale application.

The development of SIBs is still in its infancy, although the research relevant to SIBs has started in parallel with LIBs in the 1980s. The current challenge in advancing this technology lies in finding suitable electrode materials to enable reversible sodium storage. During the past decade, many sodium insertion materials have been found or revisited as candidates for electrode materials by a number of different research groups.[5,7,8] For example, various layered transition oxides (Na_xMO_2, M = Fe, Mn, Co, Ni, Cr, and V) with the O3- or P2-type structure have been systematically investigated as cathode materials for SIBs.[5] NASICON-type compounds ($Na_xM_x(PO_4)_y$, $1 \leq x < 4$, M = Ti and V) have shown good electrochemical activity with sodium in a reversible manner.[9,10] Recently, sodium titanates have been discovered as new anode materials with fairly low working potentials (<1 V) in SIBs.[11–14] Unfortunately, compared with their lithium analogues, many of these electrode materials exhibit unsatisfactory electrochemical performance in SIBs, such as low energy density, short cycling lifetime, and poor rate

[a]Department of Mechanical and Materials Engineering, University of Western Ontario, London, ON N6A 5B9, Canada. E-mail: xsun9@uwo.ca

[b]Advanced Light Source, Lawrence Berkeley National Laboratory, Berkeley, CA 94720, USA

[c]Department of Chemistry, University of Western Ontario, London, ON N6A 5B7, Canada

[d]Department of Chemistry and Biochemistry, University of California, Santa Cruz, California 95064, USA

† Electronic supplementary information (ESI) available: Experimental procedure, SEM images of sodium titanates on CNTs, Si(100) wafer and AAO template, FTIR spectra of sodium titanates and anatase TiO_2, SAED patterns of sodium titanates/CNTs as deposited at 225 °C and annealed at 500 °C in air, crystal structure of anatase TiO_2 and $Na_{0.23}TiO_2$, SEM images of sodium titanates as-deposited at 225 °C and after annealing in air at 500 °C, 700 °C, and 900 °C, SEM images of sodium titanates deposited at 275 °C on a Si wafer, Raman spectra of A-NaTiO and C-NaTiO, XRD pattern of $Na_{0.23}TiO_2$/CNTs, CV and cycling stability of CNTs, discharge capacities and TG results of A-NaTiO/CNTs and C-NaTiO/CNTs. See DOI: 10.1039/c5ta08435k

capability.[5,11–14] One main reason for this is the relatively large ionic radius of the sodium ion (1.06 Å *vs.* 0.76 Å of the lithium ion), which often leads to larger structural distortions and higher diffusion barriers in the host materials during charge/discharge cycling.[5,15] From this aspect, nanosizing electrode materials has been proven as a key strategy to address the above problem and to achieve good battery performance in SIBs.[14,16,17]

Recently, atomic layer deposition (ALD) has emerged as a powerful technique to improve the electrochemical performance of LIBs, by designing the electrode/electrolyte interface or preparing nanosized electrode materials.[18–20] Owing to the self-controlled surface reactions employed, ALD can achieve uniform and conformal film deposition on various substrates, with atomic-level controlled film thickness.[21,22] Due to these advantages, many research groups have demonstrated that ultrathin coating layers on the electrode suppress unfavorable reactions at the electrode/electrolyte interface or in the electrode materials, resulting in enhanced energy density, cycling stability, and rate capability of cathode and anode materials in LIBs.[23–26] Moreover, ALD has been applied to directly synthesize a variety of nanosized electrode materials for LIBs, including lithium-absent (metal oxides, sulfides, and phosphates),[27–30] and lithium-containing materials (such as $LiCoO_2$, Li_2MnO_4, and $LiFePO_4$).[31–33] These electrode materials have shown good electrochemical performance as anodes or cathodes in LIBs.[27–33] Furthermore, ALD has been used to fabricate an all-in-one nanopore battery array,[34] making it a promising candidate for commercial fabrication of real 3D all-solid-state microbatteries. Considering these successful applications of ALD in LIBs, it is highly expected that ALD will also play an important role in developing high-performance electrode materials for SIBs. In fact, lithium-absent materials prepared by ALD (such as metal oxides and $FePO_4$) can be directly adopted as anode or cathode materials for SIBs.[7,8] At present, a substantial challenge is how to use ALD to synthesize sodium-containing electrode materials, which account for a majority of electrode materials in SIBs.

In this work, for the first time, we developed an ALD approach to deposit sodium titanate anode materials as a representative example of sodium-containing electrode materials for SIBs. This ALD approach demonstrates excellent control over the growth rate, thickness, and composition of sodium titanates, as well as the flexibility of coating uniform and conformal sodium titanate films on substrates with various dimensions, including planar Si wafers, 1D carbon nanotubes (CNTs), and 3D anodic aluminium oxide (AAO) templates. The as-deposited sodium titanates were amorphous in nature, but could be easily transformed into a highly crystalline structure after post-annealing. A full picture of this amorphous/crystalline phase transformation process was captured by using *in situ* and *ex situ* characterization techniques. Moreover, electrochemical measurements indicated that amorphous sodium titanate exhibited higher specific capacity, better rate capability, and ultra-longer cycle lifetime than the crystalline one, making it an excellent candidate as an anode material for SIBs. This breakthrough not only provides a new approach for the fabrication of the well-defined nanostructured sodium titanate anode material, but also provides a novel methodology that can be adopted to synthesize other sodium-containing electrode materials for SIBs.

Experimental

Deposition of sodium titanates by ALD

Sodium titanates were deposited in a Savannah 100 ALD system (Ultratech/Cambridge Nanotech) by using sodium *tert*-butoxide (NaO^tBu, $NaOC(CH_3)_3$, Sigma Aldrich, 97%), titanium(IV) isopropoxide (TTIP, $Ti[OCH(CH_3)_2]_4$, Sigma Aldrich, 97%), and distilled water (H_2O) as precursors. The use of NaO^tBu as an ALD precursor was reported previously.[35] The source temperature for NaO^tBu and TTIP was 180 °C and 85 °C, respectively, while H_2O was kept at room temperature (RT). The deposition temperatures for sodium titanates were carefully chosen from 200 °C to 275 °C. Thermal decomposition of TTIP has been reported at temperatures above 275 °C,[36] while below 200 °C, NaO^tBu has insufficient reactivity with H_2O. One ALD cycle of sodium titanates was composed of the following steps: [NaO^tBu (x s pulse/10 s purge)–H_2O (y s pulse/10 s purge)] + n × [TTIP (1 s pulse/10 s purge)–H_2O (0.5 s pulse/10 s purge)], where n varies from 1 to 6, in order to tune the Na/Ti atomic ratio in the films. The recipe for TiO_2 (TTIP (1 s pulse/10 s purge)–H_2O (0.5 s pulse/10 s purge)) was directly taken from our previous work.[37] Si (100) wafers, powder-based carbon nanotubes (CNTs), nitrogen-doped CNTs grown on carbon papers, and anodic aluminium oxide (AAO, 0.2 μm pore size, 12 mm diameter, Anodisc 13, Whatman) templates were used as substrates for the deposition of sodium titanates. Before deposition, the Si (100) wafer was pre-cleaned with acetone three times, rinsed with ethanol, and subsequently blown dry with compressed air. Powder-based CNTs were refluxed in nitric acid (HNO_3, 70%) for 3 h at 120 °C, in order to functionalize the surface of CNTs and remove the residual Ni catalyst used for the growth of CNTs. Then, the treated CNTs were dispersed in ethanol in an ultrasonic bath for 30 min, and the solution mixture was dropped onto an aluminium foil. After being left in air overnight, porous CNT network films formed on the aluminium foil, which were cut into 10 cm × 10 cm pieces for further deposition of sodium titanates. NCNTs on carbon papers and AAO templates were used as received.

Physical characterization of sodium titanates

The morphology, composition, and structure of sodium titanates were characterized by using field-emission scanning electron microscopy (SEM, Hitachi S4800) equipped with energy dispersive spectroscopy (EDS), Fourier transform infrared (FTIR, Nicolet 6700 spectrometer) spectroscopy, high resolution transmission electron microscopy (HRTEM, JEOL 2010 FEG), X-ray diffraction (XRD) system (Bruker D8 Advance, Cu-K_α X-ray source), and X-ray absorption near-edge spectroscopy (XANES). High-temperature *In situ* XRD (HT-XRD) measurements (scan step of 0.02° per second) were conducted on sodium titanates grown on power-based CNTs in an air atmosphere, during either a temperature-dependent or a time-dependent annealing process. In the temperature-dependent annealing process, the sodium titanate/CNT composite was annealed at each

temperature from 400 °C to 900 °C for 1 h before a measurement was made from 10° to 50°. In the time-dependent annealing process, the sodium titanate/CNT composite was first heated from 400 °C to 900 °C, with a measurement taken from 23° to 27° at a 100 °C step. When the temperature reached 900 °C, the measurement was performed with a period of 15 min. XANES measurements were performed at the Canadian Light Source (CLS) on the Spherical Grating Monochromator (SGM) beamline for Ti L-edge, O K-edge, and Na K-edge.

Electrochemical characterization of sodium titanates

Electrochemical measurements were performed on two types of sodium titanates grown on CNTs. One was amorphous sodium titanate on CNTs (denoted as A-NaTiO), which was deposited at 225 °C by using 300 ALD cycles of [NaO^tBu (4 s pulse/10 s purge)–H_2O (0.5 s pulse/10 s purge)] + 1 × [TTIP (1 s pulse/10 s purge)–H_2O (0.5 s pulse/10 s purge)]. The other was $Na_{0.23}TiO_2$ (designated as C-NaTiO) on CNTs obtained by annealing A-NaTiO in an Ar atmosphere for 10 h. The loadings of A-NaTiO and C-NaTiO were measured to be 54 wt% and 40 wt%, respectively, by using thermogravimetric analysis (TGA, SDT Q600) from RT to 800 °C in air at a heating rate of 10 °C min^{-1}. The electrochemical performance of A-NaTiO and C-NaTiO was evaluated in coin-type half cells (CR2032). To prepare the electrode, A-NaTiO or C-NaTiO on CNTs, acetylene black, and polyvinylidene fluoride (PVDF) with a weight ratio of 8 : 1 : 1 were added into an *N*-methylpyrrolidinone (NMP) solvent and ground thoroughly, and then the slurry was pasted onto a copper foil. The electrode was dried under vacuum at 100 °C overnight. The coin-type half cells were assembled in an argon-filled glovebox ([O_2] < 1 ppm, [H_2O] < 1 ppm), using the electrode prepared as above, polypropylene separator (Celgard 3501), and sodium metal as the counter electrode. The electrolyte was 1 M $NaClO_4$ in ethylene carbonate (EC) and propylene carbonate (PC) in a volume ratio of 1 : 1. Charge–discharge cycling in a constant current mode was carried out on an Arbin BT-2000 Battery Test System, and cyclic voltammetry (CV) was tested on a versatile multichannel potentiostat 3/Z (VMP3). The electrochemical performance was measured in a voltage range of 0.1–2.5 V at RT. The specific capacity was calculated in two ways. Discharge capacities of A-NaTiO/CNT and C-NaTiO/CNT composites were calculated using the following equation:

$$\text{Discharge capacity}_{\text{NaTiO+CNTs}} = \text{total capacity/weight of NaTiO/CNT composite} \quad (1)$$

Discharge capacities of only A-NaTiO and C-NaTiO were obtained by subtracting the contribution of CNTs from the total capacity using the following equation:

$$\text{Discharge capacity}_{\text{NaTiO}} = \{\text{discharge capacity}_{\text{NaTiO+CNTs}} - \text{discharge capacity}_{\text{CNTs}} \times \text{CNT loading}\}/\text{NaTiO loading} \quad (2)$$

The discharge capacity of pure CNTs is shown in the ESI.† The loadings of CNTs and NaTiO were obtained by TG analysis. Discharge $\text{capacity}_{\text{NaTiO}}$ was mainly used to compare the electrochemical performance of A-NaTiO and C-NaTiO, while discharge $\text{capacity}_{\text{NaTiO+CNTs}}$ was used to compare the performance of A-NaTiO/CNT and C-NaTiO/CNT composites.

Results and discussion

Fig. 1a illustrates the process for one ALD cycle of sodium titanates by using NaO^tBu, TTIP, and H_2O as precursors. The ALD cycle is executed by sequential pulsing of NaO^tBu, H_2O, TTIP, and H_2O, with an N_2 gas purge following each pulse, to remove excess precursor and reaction by-products. One ALD cycle consists of two ALD subcycles, *i.e.* NaO^tBu–H_2O and TTIP–H_2O, and is expressed as (NaO^tBu–H_2O) + (TTIP–H_2O) henceforth. CNTs, Si wafers, and AAO templates are employed as substrates for the deposition of sodium titanates. By repeating the ALD cycle in Fig. 1a, sodium titanate thin films are uniformly coated on the surface of nitrogen-doped CNTs, Si wafers, and in the nanopores of AAO membranes (Fig. 1b–d, and S1†). Moreover, sodium titanate films are also observed on the surface along the inner-pore walls of AAO membranes (Fig. S1†). Thus, the ALD process has a good ability to deposit high-quality sodium titanate thin films on substrates with various dimensions, making it very promising for the fabrication of 2D and 3D all-solid-state SIBs in future.

The ALD growth characteristics of sodium titanate thin films are examined on a standard Si substrate (Fig. 2). The ALD recipe for the TTIP–H_2O subcycle is directly taken from our previous work,[37] while the pulse time for NaO^tBu and H_2O in the NaO^tBu–H_2O subcycle is optimized herein, by changing one at a time while keeping the other constant. Fig. 2a and b show the

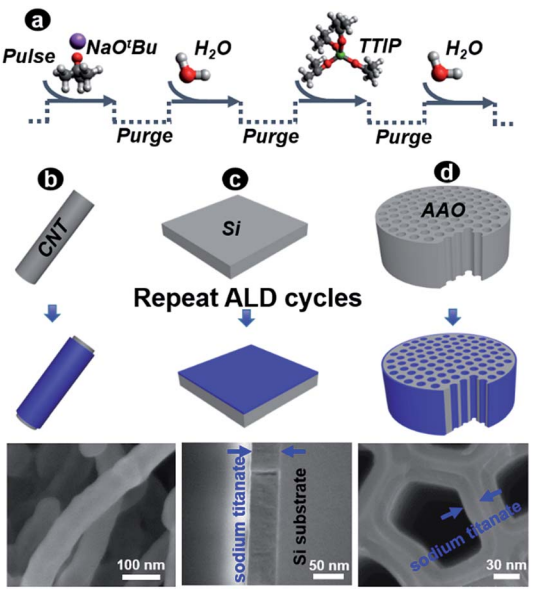

Fig. 1 (a) One ALD cycle of sodium titanates consists of a sequential pulse of NaO^tBu, H_2O, TTIP, and H_2O, with an N_2 gas purge after each pulse. By repeating the above sequence in a cyclic manner, uniform, conformal sodium titanate films (blue colour) are deposited on (b) nitrogen-doped CNTs, (c) Si wafer, and (d) AAO template (surface polished with sandpapers).

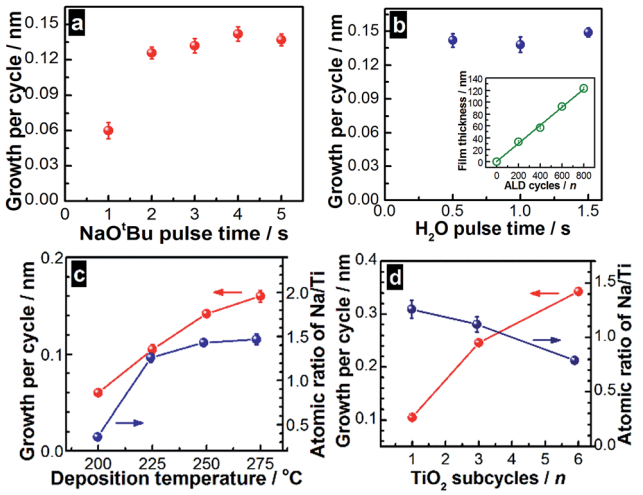

Fig. 2 Growth per cycle (GPC) of sodium titanate thin films as a function of (a) NaO^{t}Bu pulse time and (b) H_2O pulse time at 250 °C using the ALD recipe of (NaO^{t}Bu–H_2O) + (TTIP–H_2O) (inset in Fig. 2b displays the film thickness of sodium titanates as a function of ALD cycle number); the dependence of the GPC and Na/Ti atomic ratio of sodium titanates (c) on deposition temperatures using the ALD recipe of (NaO^{t}Bu–H_2O) + (TTIP–H_2O), and (d) on TiO_2 subcycles at 225 °C using ALD recipes of (NaO^{t}Bu–H_2O) + n × (TTIP–H_2O) (n = 1, 3, and 6).

dependence of growth per cycle (GPC) of sodium titanate thin films at 250 °C on NaO^{t}Bu and H_2O pulse time, respectively. The GPC of sodium titanate films increases with NaO^{t}Bu pulse time, and saturates at ~0.14 nm with NaO^{t}Bu pulse of 4 s or longer (Fig. 2a), whereas the GPC of sodium titanate films remains unchanged, with H_2O pulse time varying from 0.5 s to 1.5 s (Fig. 2b). Thus, a pulse duration of 4 s and 0.5 s will be used for NaO^{t}Bu and H_2O, respectively, in order to achieve saturated growth of sodium titanate films during the ALD process. Moreover, the film thickness of sodium titanates shows a linear relationship with the ALD cycle number, yielding a GPC of 0.15 nm for sodium titanates at 250 °C (inset in Fig. 2b). Assuming a GPC of ~0.03 nm for the TTIP–H_2O subcycle,[36,37] a growth rate of 0.12 m per cycle is obtained for the NaO^{t}Bu–H_2O subcycle at 250 °C. Such a high growth rate was also observed in ALD of LiO^{t}Bu–H_2O (~0.17 nm per cycle at 225 °C).[38,39] The reason for the high growth rate might be due to physisorption of H_2O (as seen in FTIR spectra in Fig. S2†) on the layer(s) produced during the NaO^{t}Bu–H_2O subcycle (possibly NaOH or sodium oxide), as a result of their hygroscopic nature.[38,40] Residual water would react with TTIP or NaO^{t}Bu in the subsequent subcycle, resulting in a higher GPC of sodium titanate films. The results in Fig. 2a and b justify the true ALD process used for the deposition of sodium titanates. Fig. 2c shows the growth behaviour and composition of sodium titanate films at different temperatures. The GPC of sodium titanate films turns out to be 0.06 nm, 0.11 nm, 0.15 nm, and 0.16 nm, at temperatures of 200 °C, 225 °C, 250 °C, and 275 °C, respectively. The Na/Ti atomic ratio in sodium titanate films was determined by EDS analysis and found to be around 1.4 between 225 °C and 275 °C, and reduced to 0.4 at 200 °C, suggesting decreased reactivity between NaO^{t}Bu and H_2O below 225 °C. Fig. 2d illustrates that the composition of sodium titanates can be tuned by adjusting the ALD recipe, *i.e.* adding more TTIP–H_2O subcycles. The modified ALD recipe is expressed as (NaO^{t}Bu–H_2O) + n × (TTIP–H_2O), where n equals 1, 3, and 6. The Na/Ti atomic ratio decreases from 1.3 to 1.1 and 0.8, with TTIP–H_2O subcycles elevating from 1, to 3 and 6, respectively (Fig. 2d). The above results demonstrate good controllability of the ALD process over the growth rate, thickness, and composition of sodium titanate films.

Sodium titanates prepared by ALD show an amorphous structure in the as-deposited state, as revealed by the XRD pattern in Fig. 3a and HRTEM image in Fig. 3d (Fig. S3a† for the selected-area electron diffraction (SAED) pattern). To obtain crystalline sodium titanates, HT-XRD measurements were carried out on the sodium titanates as-deposited on CNTs (sodium titanates/CNTs) at 225 °C. Fig. 3a and b illustrate the crystallization of sodium titanates during temperature- and time-dependent annealing processes, respectively. As seen in Fig. 3a, XRD patterns of sodium titanates/CNTs at RT shows only three distinct peaks at 26°, 43°, and 44° (labelled as +), assigned to (002), (100), and (101) planes of graphite (JCPDS no.

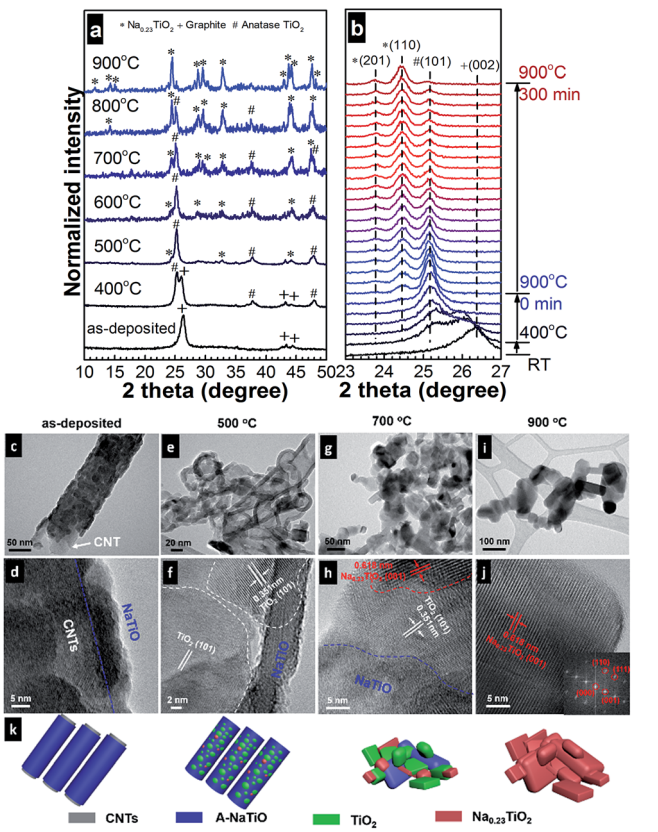

Fig. 3 HT-XRD measurements of sodium titanates/CNTs in (a) a temperature-dependent annealing process from 400 °C to 900 °C, and (b) a time-dependent annealing process at 900 °C in air (* $Na_{0.23}TiO_2$, JCPDS no. 22-1404; + graphite, JCPDS no. 08-0415; # anatase TiO_2, JCPDS no. 02-0387); TEM and HRTEM images of sodium titanates/CNTs (c and d) under the as-deposited conditions, and after annealing at (e and f) 500 °C, (g and h) 700 °C, (i and j) 900 °C in an air atmosphere; (k) schematic diagram of structural and morphological evolution of sodium titanates/CNTs with increasing annealing temperature.

08-0415), respectively. After annealing the sodium titanate/CNT composite at 400 °C for 1 h in air, one strong peak at 25°, followed by two weak peaks at 38° and 48° (marked as #) can be found and attributed to the (101), (004), and (200) planes of anatase TiO_2 (JCPDS no. 02-0387). Heat treatment at 500 °C leads to the loss of graphitic peaks as a result of CNT combustion in air. Besides the dominant peaks from anatase TiO_2, several weak diffraction peaks show up at 24°, 33°, and 44° (marked as *), which correspond to (110), (002), and (003) planes of monoclinic $Na_{0.23}TiO_2$ (JCPDS no. 22-1404), respectively. Annealing from 500 °C to 800 °C results in a steady increase in peaks associated with $Na_{0.23}TiO_2$, and a gradual decrease in intensity of anatase TiO_2 peaks. Interestingly, all the peaks in the XRD pattern for the 900 °C annealed sodium titanate/CNT composite can be assigned to monoclinic $Na_{0.23}TiO_2$. The HT-XRD results taken during time-dependent annealing at 900 °C (Fig. 3b) show the same trend of phase transition as shown in Fig. 3a. Moreover, Fig. 3b indicates that a minimum annealing time of 300 min is required in order to obtain pure monoclinic $Na_{0.23}TiO_2$ at 900 °C. Furthermore, the HT-XRD results reveal that amorphous sodium titanates can be transformed into crystalline $Na_{0.23}TiO_2$ at 900 °C, through an intermediate phase of anatase TiO_2. The crystal structures of anatase TiO_2 and $Na_{0.23}TiO_2$ are shown in Fig. S4.†

Microstructural evolution from amorphous sodium titanates to $Na_{0.23}TiO_2$ is determined by *ex situ* microscopic observations on the samples annealed at different temperatures (Fig. 3c–j for TEM and HRTEM images and Fig. S5† for SEM images). Prior to heat treatment, the surface of the CNTs is evenly covered with the ALD of amorphous sodium titanate films (Fig. 3c and d). Annealing at temperatures below 500 °C leads to rapid nucleation and growth of nanocrystalline anatase TiO_2 in the matrix of amorphous sodium titanates (Fig. 3f and S3b†). At 500 °C, the burning of CNTs in air leads to the formation of hollow sodium titanates (Fig. 3e). With increasing annealing temperature, the hollow structured sodium titanate further breaks down into irregular nanoparticles. Meanwhile, crystalline $Na_{0.23}TiO_2$ begins nucleating alongside anatase TiO_2 (Fig. 3g and h), most likely through the diffusion of sodium ions in surrounding areas into anatase TiO_2. Highly crystalline $Na_{0.23}TiO_2$ nanoparticles with sizes of ~100–300 nm are formed eventually at 900 °C (Fig. 3i and j). Fig. 2k schematically illustrates structural and morphological evolution from amorphous sodium titanates to $Na_{0.23}TiO_2$ with increasing annealing temperature.

Amorphous and crystalline sodium titanates are analysed by using the X-ray absorption spectroscopy technique, which is highly sensitive to the symmetry and local chemical environment around a specific element.[41,42] Fig. 4 presents XANES spectra at Ti $L_{2,3}$-edge, O K-edge, and Na K-edge for amorphous sodium titanates deposited at different temperatures, $Na_{0.23}TiO_2$, and anatase TiO_2. The Ti $L_{2,3}$-edge spectra of all the samples show two groups of peaks arising from the spin–orbit splitting of the Ti 2p core level into $2p_{3/2}$ (L_3-edge) and Ti $2p_{1/2}$ levels (L_2-edge).[42–44] At both the L_3-edge and L_2-edge, the crystal field splits the 3d band into t_{2g} and e_g sub-bands. The most prominent difference among the as-deposited sodium titanates and $Na_{0.23}TiO_2$ is the split of the fine structure in the L_3-e_g band,

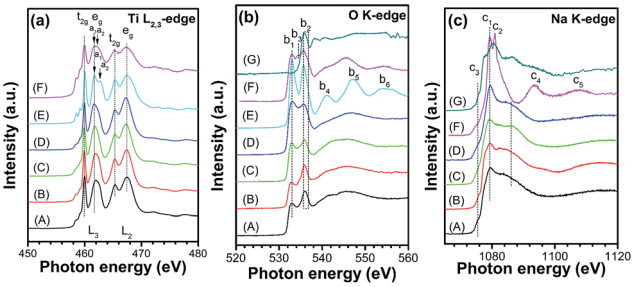

Fig. 4 XANES spectra at (a) Ti $L_{2,3}$-edge, (b) O K-edge, and (c) Na K-edge for sodium titanates deposited by ALD at (A) 275 °C, (B) 250 °C, (C) 225 °C, and (D) 200 °C, (E) anatase TiO_2 deposited by ALD at 225 °C, (F) $Na_{0.23}TiO_2$, and (G) standard Na_2CO_3.

which is highly sensitive to the local symmetry (distortion from O_h) around the metal cations.[45] All the as-deposited sodium titanates show broadening at the e_g peaks associated with the L_3-edge (Fig. 4a(A–D)), which are indicative of a highly disordered and amorphous sample.[42,44] The broadened peak is attributed to the loss of long-range order due to the effects of titanium interactions with second-neighbouring atoms.[42] The peak attributed to the L_3-e_g band shifts to a slightly higher energy in sodium titanates deposited at a higher temperature. This is most likely due to the different Na/Ti atomic ratios in the sodium titanate films (Fig. 2c). In contrast, $Na_{0.23}TiO_2$, as well as anatase TiO_2, shows two well-resolved peaks of e_g orbitals in the L_3-edge (labelled as a_1 and a_2 in Fig. 4a(E and F)), suggesting their highly crystalline structure. Previous work has shown that each structure has its own characteristics in terms of the relative intensity between a_1 and a_2 peaks and the value of their energy splitting at the e_g orbitals in the L_3-edge.[42,44,45] For example, the intensity of the a_1 peak (461.7 eV) is substantially stronger than that of the a_2 peak (462.7 eV) for anatase TiO_2 (as shown in Fig. 4a(E)), while the trend is opposite in rutile TiO_2.[42,44] For $Na_{0.23}TiO_2$, the a_1 and a_2 peaks show almost identical peak intensities along with a 0.5 eV energy splitting, which can be used as characteristic features to identify this structure in the future.

O K-edge absorption involves the excitation of a 1s electron in oxygen into an unoccupied 2p orbital.[45] O K-edge spectra of all the samples in Fig. 4b (except Na_2CO_3) show two dominant features within an energy range of 530–536 eV, which can be assigned to the transitions into O states hybridized with Ti 3d t_{2g} and e_g levels (marked as b_1 and b_2 in Fig. 4b).[42,45] The broadening feature displayed in the as-deposited sodium titanates (Fig. 4b(A–D)), compared to crystalline anatase TiO_2 for example, are inherent to the amorphous structure of the sample, and is caused by slight variations in bond lengths and angles.[44] It is noteworthy that the b_2 peaks for sodium titanate deposited at 200 °C, $Na_{0.23}TiO_2$, and anatase TiO_2 (Fig. 4b(D–F)) are centred at 535.6 eV, while b_2 peaks for sodium titanates deposited at 225 °C, 250 °C, and 275 °C (Fig. 4b(A–C)) shift to a higher energy of 535.9 eV, which agrees well with that of standard Na_2CO_3 (Fig. 4b(G)). Therefore, the b_2 peaks in Fig. 4b(A–C) are partially contributed by Na_2CO_3, which is found to exist on the top surface of sodium titanates on the Si wafer

(see the SEM image in Fig. S6†). Interestingly, the intensity of the b_2 peak in Fig. 4b(A–C) can be correlated with increasing ALD deposition temperatures, indicating the formation of greater amounts of Na_2CO_3 impurity at higher temperatures. The Na_2CO_3 impurity might be formed as a result of reactions between the Na–O layers and CO_2 in the atmosphere, when the samples are taken out of the ALD reaction chamber (similar phenomenon to that observed in the ALD process of LiO^tBu–H_2O).[38–40] $Na_{0.23}TiO_2$ shows several differences from anatase TiO_2 at the O K-edge. In the low energy region, $Na_{0.23}TiO_2$ shows higher peak intensity of b_2 than b_1 (the opposition in anatase TiO_2), and one additional peak (b_3) at 534.4 eV. At a higher energy, b_4 and b_5 peaks detected in anatase TiO_2 merge into a single asymmetric peak in $Na_{0.23}TiO_2$, while the b_6 peak in $Na_{0.23}TiO_2$ becomes suppressed. The line-shape of $Na_{0.23}TiO_2$ is somehow similar to that of sodium titanate nanotubes from a previous work.[45] Based on experimental and calculation studies, the difference between sodium titanates and TiO_2 is mainly due to the existence of more types of oxygen sites in the former (as also revealed by Raman spectra in Fig. S7†), which can affect the O–Ti coordination number and the connectivity of the octahedral.[45]

Turning to the Na K-edge, we can see that the as-deposited sodium titanates present a very broad doublet between 1076 eV and 1094 eV (Fig. 4c(A–D)), which is typical of short-range ordering around sodium.[46–48] In contrast, the absorption spectrum of $Na_{0.23}TiO_2$ displays sharper peaks with greater intensity (Fig. 4c(F)) at 1075.3 eV (c_3), 1079.3 eV (c_1), 1081.0 eV (c_2), 1093.8 eV (c_4), and 1107.0 eV (c_5), suggesting that the environment around the sodium element contains greater periodicity than that in the as-deposited sodium titanates. Based on the above XANES results, we can find that all the as-deposited sodium titanates have a disordered structure, and show some minor differences in the local environment around titanium and oxygen. A small amount of Na_2CO_3 is detected on the surface of sodium titanates prepared at temperatures above 225 °C. Post-annealing in air leads to a much more ordered structure in $Na_{0.23}TiO_2$ than in the as-deposited sodium titanates.

Electrochemical measurements were performed on amorphous sodium titanate (denoted as A-NaTiO) and crystalline $Na_{0.23}TiO_2$ (denoted as C-NaTiO) deposited on CNTs. In order to maintain the CNT structure, C-NaTiO is obtained by annealing A-NaTiO for 10 h in Ar gas. A-NaTiO is uniformly coated on the whole surface of CNTs (Fig. 5a), while C-NaTiO contains nanoparticles with sizes of 100–300 nm located on CNTs (Fig. 5b, and its phase is confirmed by XRD in Fig. S8†). The HRTEM image in the inset of Fig. 5b discloses a highly crystalline structure of $Na_{0.23}TiO_2$ nanoparticles. Fig. 5c and d display cyclic voltammetry (CV) curves of A-NaTiO and C-NaTiO in the first three cycles. A-NaTiO exhibits an irreversible peak at 0.38 V in the first discharge cycle, which is attributed to the formation of a solid electrolyte interphase (SEI),[11,14] and broad charge/discharge peaks between 0.1 and 1 V in the subsequent cycles. Interestingly, the first-cycle CV curve of C-NaTiO is quite different from the subsequent cycles with the appearance of two additional peaks from 1.44 to 1.99 V. From the second cycle, C-NaTiO exhibits two groups of reduction/oxidation peaks at 1.93 V/2.18 V and 0.81 V/1.60 V, respectively, suggesting a two-step insertion/extraction process for sodium ions in $Na_{0.23}TiO_2$ host, albeit the exact reaction mechanisms are not clear yet. From Fig. 5c, it is also clear that the electrochemical potential of A-NaTiO is below 1 V, which is comparable to other types of sodium titanates.[12–14,49,50] Such low potential of sodium titanates would provide a higher energy density of full cells, compared to their lithium counterpart (such as $Li_4Ti_5O_{12}$, ~1.5 V potential).[51] Fig. 5e shows the cycling performance of A-NaTiO and C-NaTiO at a current density of 10 mA g^{-1}. Since pure CNTs show a reversible sodium storage capacity of ~30 mA h g^{-1} at 10 mA g^{-1} (Fig. S9†), discharge capacities of A-NaTiO and C-NaTiO (Fig. 5e) were obtained by subtracting contribution of CNTs from total capacities of A-NaTiO/CNT and C-NaTiO/CNT composites (Fig. S10†) using eqn (1) and (2) described in

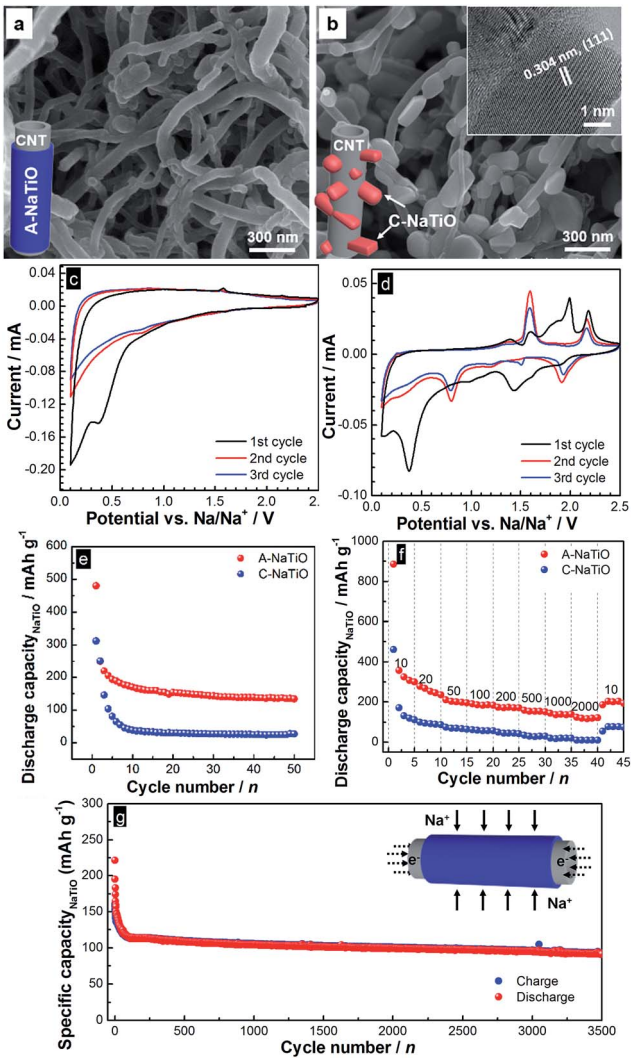

Fig. 5 SEM images of amorphous sodium titanate (A-NaTiO) (a) and crystalline $Na_{0.23}TiO_2$ (C-NaTiO) (b) on CNTs; CV curves of (c) A-NaTiO and (d) C-NaTiO measured between 0.1 V and 2.5 V at a scan rate of 0.1 mV s^{-1}; (e) cycling performance of A-NaTiO and C-NaTiO at a current rate of 10 mA g^{-1}; (f) rate capability of A-NaTiO and C-NaTiO at current rates of 20–2000 mA g^{-1}; and (g) long-cycle life of A-NaTiO at 500 mA g^{-1}.

Experimental (Fig. S11† for the TGA results of A-NaTiO/CNTs and C-NaTiO/CNTs). As seen in Fig. 5e, A-NaTiO exhibits a discharge capacity of$\sim$ 483 mA h g^{-1} in the first cycle, which gradually decreases and stabilizes at $\sim$140 mA h g^{-1} after 20 cycles. C-NaTiO shows a similar trend to A-NaTiO, but with a much lower capacity. For example, C-NaTiO shows a discharge capacity of 315 mA h g^{-1} in the first cycle, and a stable capacity of 28 mA h g^{-1} after the 50th cycles, which is only one fifth of that of A-NaTiO. As a result, the A-NaTiO/CNT composite also shows a higher capacity than the C-NaTiO/CNT composite (Fig. S10†). Fig. 5f compares the rate capabilities of A-NaTiO and C-NaTiO at current densities from 10 mA g^{-1} to 2000 mA g^{-1}. It is clear that A-NaTiO exhibits a much higher capacity than C-NaTiO at each current density. A-NaTiO can deliver a discharge capacity of $\sim$98 mA h g^{-1} even at 2000 mA g^{-1}, while C-NaTiO only exhibits a capacity of 10 mA h g^{-1} for C-NaTiO at the same current density. A-NaTiO on CNTs in this work exhibits superior rate capability compared with sodium titanates reported previously (Fig. S12†). Furthermore, the long-term cycling performance of A-NaTiO is evaluated at 500 mA g^{-1} (Fig. 5g). The capacity of A-NaTiO quickly drops from 197 mA h g^{-1} to 114 mA h g^{-1} in the first 100 cycles, and becomes stable afterward. A-NaTiO can still maintain a discharge capacity of 100 mA h g^{-1} even after 3500 cycles. Previous work has demonstrated that sodium titanates generally suffered from poor cycling performance.[12–14,49,50] To the best of our knowledge, such ultra-long cycling lifetime of A-NaTiO has never been reported so far. In addition, it is further found that the A-NaTiO/CNT electrode prepared without acetylene black can still deliver a high discharge capacity which is just slightly lower than the electrode made with 10 wt% acetylene black (Fig. S13†), indicating that the CNT network already has good electronic conductivity to ensure acceptable sodium insertion/extraction. The waiver of acetylene black in the electrode will increase the energy density of battery cells. The excellent electrochemical performance of A-NaTiO can be attributed to the synergies of the A-NaTiO/CNT shell/core structure designed by ALD: (i) the thin A-NaTiO layer uniformly coated on CNTs ensures fast sodium ion diffusion into/out of the host material; (ii) the highly conductive CNT substrates allow for rapid electron transport to the A-NaTiO active material (schematically shown in the inset of Fig. 5g); and (iii) the amorphous nature of A-NaTiO can better accommodate structural distortion that occurs during sodium insertion/extraction.[35,52,53] At last, it is worth pointing out that the controllability of this ALD process on the composition of amorphous sodium titanates (Fig. 2c and d) makes it possible to obtain sodium titanates with various Na/Ti stoichiometric ratios and phases, which have been shown to exhibit quite different sodium storage behaviours.[12–14,49,50]

Conclusions

In conclusion, sodium titanate thin films have been successfully deposited using the ALD technique by combination of NaO^tBu–H_2O and TTIP–H_2O subcycles. The sodium titanate thin films were well controllable in growth rate, film thickness, and composition, and could be applied to various types of substrates. Crystalline $Na_{0.23}TiO_2$ was obtained after post-annealing. Synchrotron XAS measurements were adopted to elucidate the chemical and local environment of Na, O, and Ti elements in both amorphous and crystalline sodium titanates. Amorphous sodium titanates deposited on CNTs exhibited exceptional battery performance as anode materials for SIBs, including high energy density, excellent rate capability, and ultra-long cycling life. These advantages of sodium titanates synthesized by ALD make them competitive anode materials for high-powered SIBs. Furthermore, the ALD approach developed herein can be extended to fabricate other sodium-containing electrode materials in SIBs. We believe that this work paves a new pathway towards well-defined synthesis of electrode materials for rechargeable sodium batteries.

Acknowledgements

This work was supported by the Nature Sciences and Engineering Research Council of Canada (NSERC), Canada Research Chair (CRC) Program, Canada Foundation of Innovation (CFI), Ontario Research Fund (ORF), the Canadian Light Source (CLS) at University of Saskatchewan, the Canadian Centre for Electron Microscopy (CCEM) at McMaster University, and the University of Western Ontario. Dr Guo's work at the ALS is supported by the Director, Office of Science, Office of Basic Energy Sciences, of the U.S. Department of Energy under Contract No. DE-AC02-05CH11231. Dr Jian Liu is really grateful to the financial support from the NSERC Postdoctoral Fellowships (PDF) Program.

Notes and references

1 J. B. Dunn, L. Gaines, J. C. Kelly, C. James and K. G. Gallagher, *Energy Environ. Sci.*, 2015, **8**, 158.
2 Y. Jiang, Y. Li, W. Sun, W. Huang, J. Liu, B. Xu, C. Jin, T. Ma, C. Wu and M. Yan, *Energy Environ. Sci.*, 2015, **8**, 1471.
3 Y. Li, S. Yu, T. Yuan, M. Yan and Y. Jiang, *J. Power Sources*, 2015, **282**, 1.
4 M. D. Slater, D. Kim, E. Kee and C. S. Johnson, *Adv. Funct. Mater.*, 2013, **23**, 947.
5 N. Yabuuchi, K. Kubota, M. Dahbi and S. Komaba, *Chem. Rev.*, 2014, **114**, 11636.
6 H. Pan, Y. S. Hu and L. Chen, *Energy Environ. Sci.*, 2013, **6**, 2338.
7 S.-W. Kim, D.-H. Seo, X. Ma, G. Ceder and K. Kang, *Adv. Energy Mater.*, 2012, **2**, 710.
8 F. Klein, B. Jache, A. Bhide and P. Adelhelm, *Phys. Chem. Chem. Phys.*, 2013, **15**, 15876.
9 C. Delmas and A. Nadiri, *Solid State Ionics*, 1988, **28**, 419.
10 L. S. Plashnitsa, E. Kobayashi, Y. Noguchi, S. Okada and J.-I. Yamaki, *J. Electrochem. Soc.*, 2010, **157**, A536.
11 P. Senguttuvan, G. Rousse, V. Seznec, J.-M. Tarascon and M. R. Palacín, *Chem. Mater.*, 2011, **23**, 4109.
12 D. Wu, X. Li, B. Xu, N. Twu, L. Liu and G. Ceder, *Energy Environ. Sci.*, 2015, **8**, 195.
13 K. Shen and M. Wagemaker, *Inorg. Chem.*, 2014, **53**, 8250.
14 H. Pan, X. Lu, X. Yu, Y.-S. Hu, H. Li, X.-Q. Yang and L. Chen, *Adv. Energy Mater.*, 2013, **3**, 1186.

15 M. Gu, A. Kushima, Y. Shao, J.-G. Zhang, J. Liu, N. D. Browning, J. Li and C. Wang, *Nano Lett.*, 2013, **13**, 5203.
16 X. Yu, H. Pan, W. Wan, C. Ma, J. Bai, Q. Meng, S. N. Ehrlich, Y.-S. Hu and X.-Q. Yang, *Nano Lett.*, 2013, **13**, 4721.
17 G. Hasegawa, K. Kanamoni, T. Kiyomura, H. Kurata, K. Nakanishi and T. Abe, *Adv. Energy Mater.*, 2015, **5**, 1400730.
18 J. Liu and X. Sun, *Nanotechnology*, 2015, **26**, 024001.
19 X. Meng, X.-Q. Yang and X. Sun, *Adv. Mater.*, 2012, **24**, 3589.
20 H. C. M. Knoops, M. E. Donders, M. C. M. van de Sanden, P. H. L. Notten and W. M. M. Kessels, *J. Vac. Sci. Technol.*, 2012, **30**, 010801.
21 V. Miikkulainen, M. Leskelä, M. Ritala and R. L. Puurunen, *J. Appl. Phys.*, 2013, **113**, 021301.
22 S. M. George, *Chem. Rev.*, 2010, **110**, 111.
23 I. D. Scott, Y. S. Jung, A. S. Gavanagh, Y. Yan, A. C. Dillon, S. M. George and S.-H. Lee, *Nano Lett.*, 2011, **11**, 414.
24 X. Li, J. Liu, X. Meng, Y. Yang, M. N. Banis, J. Yang, Y. Hu, R. Li, M. Cai and X. Sun, *J. Power Sources*, 2014, **247**, 57.
25 D. Wang, J. Yang, J. Liu, X. Li, R. Li, M. Cai, T.-K. Sham and X. Sun, *J. Mater. Chem. A*, 2014, **2**, 2306.
26 Y. He, X. Yu, Y. Wang, H. Li and X. Huang, *Adv. Mater.*, 2011, **23**, 4938.
27 X. Li, X. Meng, J. Liu, D. Geng, Y. Zhang, M. N. Banis, Y. Li, J. Yang, R. Li, X. Sun, M. Cai and M. W. Verbrugge, *Adv. Funct. Mater.*, 2012, **22**, 1647.
28 X. Meng, J. A. Libera, T. T. Fister, H. Zhou, J. K. Hedlund, P. Fenter and J. W. Elam, *Chem. Mater.*, 2014, **26**, 1029.
29 K. B. Gandrud, A. Pettersen, O. Nilsen and H. Fjellvåg, *J. Mater. Chem. A*, 2013, **1**, 9054.
30 J. Liu, B. Xiao, M. N. Banis, R. Li, T.-K. Sham and X. Sun, *Electrochim. Acta*, 2015, **162**, 275–281.
31 M. E. Donders, W. M. Arnoldbik, H. C. M. Knoops, W. M. M. Kessels and P. H. L. Notten, *J. Electrochem. Soc.*, 2013, **160**, A3066.
32 V. Miikkulainen, A. Ruud, E. Østreng, O. Nilsen, M. Laitinen, T. Sajavaara and H. Fjellvåg, *J. Phys. Chem. C*, 2014, **118**, 1258.
33 J. Liu, M. N. Banis, Q. Sun, A. Lushington, R. Li, T.-S. Sham and X. Sun, *Adv. Mater.*, 2014, **26**, 6472.
34 C. Liu, E. I. Gillette, X. Chen, A. J. Pearse, A. C. Kozen, M. A. Schroeder, K. E. Gregorczyk, S. B. Lee and G. W. Rubloff, *Nat. Nanotechnol.*, 2014, **9**, 1031.
35 E. Østreng, H. H. Sønsteby, S. Øien, O. Nilsen and H. Fjellvåg, *Dalton Trans.*, 2014, **43**, 16666.
36 M. Ritala and M. Keskelä, *Chem. Mater.*, 1993, **5**, 1174.
37 X. Meng, D. Geng, J. Liu, R. Li and X. Sun, *Nanotechnology*, 2011, **22**, 165602.
38 T. Aaltonen, O. Nilsen, A. Magrasó and H. Fjellvåg, *Chem. Mater.*, 2011, **23**, 4669.
39 J. Liu, M. N. Banis, X. Li, A. Lushington, M. Cai, R. Li, T.-K. Sham and X. Sun, *J. Phys. Chem. C*, 2013, **117**, 20260.
40 A. S. Cavanagh, Y. Lee, B. Yoon and S. M. George, *ECS Trans.*, 2010, **33**, 223.
41 S. Yang, D. Wang, G. Liang, Y. M. Yiu, J. Wang, L. Liu, X. Sun and T.-K. Sham, *Energy Environ. Sci.*, 2012, **5**, 7007.
42 M.-Y. Hsu, W.-C. Yang, H. Teng and J. Leu, *J. Electrochem. Soc.*, 2011, **158**, K81.
43 J. G. Zhou, H. T. Fang, J. M. Maley, M. W. Murphy, J. Y. Peter Ko, J. N. Cutler, R. Sammynaiken, T. K. Sham, M. Liu and F. Li, *J. Mater. Chem.*, 2009, **19**, 6804.
44 S. O. Kucheyeu, T. van Buuren, T. F. Baumann, J. H. Satcher Jr, T. M. Willey, R. W. Meulenberg, T. E. Felter, J. F. Poco, S. A. Gammon and L. J. Terminello, *Phys. Rev. B: Condens. Matter Mater. Phys.*, 2004, **69**, 245102.
45 C. Bittencourt, P. Krüger, M. J. Lagos, X. Ke, G. V. Tendeloo, C. Ewels, P. Umek and P. Guttmann, *Beilstein J. Nanotechnol.*, 2012, **3**, 789.
46 S. D. Wispelaere, D. Cabaret, C. Levelut, S. Rossano, A.-M. Flank, P. Parent and F. Farges, *Chem. Geol.*, 2004, **213**, 63.
47 L. Cormier and D. R. Neuville, *Chem. Geol.*, 2004, **213**, 103.
48 D. R. Neuville, L. Cormier, A.-M. Flank, R. J. Prado and P. Lagarde, *Eur. J. Mineral.*, 2004, **16**, 809.
49 A. Rudola, K. Saravanan, C. W. Mason and P. Balaya, *J. Mater. Chem. A*, 2013, **1**, 2653.
50 W. Wang, C. Yu, Y. Liu, J. Hou, H. Zhu and S. Jiao, *RSC Adv.*, 2013, **3**, 1041.
51 J. Liu, X. Li, J. Yang, D. Geng, Y. Li, D. Wang, R. Li, X. Sun, M. Cai and M. W. Verbrugge, *Electrochim. Acta*, 2012, **63**, 100.
52 E. Uchaker, Y. Z. Zheng, S. Li, S. L. Candelaria, S. Hu and G. Z. Cao, *J. Mater. Chem. A*, 2014, **2**, 18208.
53 W. Wang, S. Wang, H. Jiao, P. Zhan and S. Jiao, *Phys. Chem. Chem. Phys.*, 2015, **17**, 4551.

